Corrosion Science 258 (2026) 113395

Contents lists available at ScienceDirect

Corrosion Science

journal homepage: www.elsevier.com/locate/corsci

Prism-plane-textured Cr_2AlC MAX-phase coatings with superior resistance to coupled thermal–salt–steam corrosion

Kaixuan Xu [a], Shenghao Zhou [a], Zhenyu Wang [a,*], Xiaoyu Sun [a], Kaiwei Yang [a,b], Kaihang Wang [a,b], Aiying Wang [a,b], Peiling Ke [a,b,**]

[a] State Key Laboratory of Advanced Marine Materials, Zhejiang Key Laboratory of Extreme-environmental Material Surfaces and Interfaces, Ningbo Institute of Materials Technology and Engineering, Chinese Academy of Sciences, Ningbo 315201, China
[b] Center of Materials Science and Optoelectronics Engineering, University of Chinese Academy of Sciences, Beijing 100049, China

A R T I C L E I N F O

Keywords:
Cr_2AlC coating
MAX phase
Strong prism plane texture
Synchronized pulsed HiPIMS
Thermal–salt–steam corrosion

A B S T R A C T

Conventional protective coatings tend to fail prematurely under the extreme thermal–salt–steam coupled conditions typical of marine and aero-engine operating environments. Here, we present a strategy to enhance corrosion resistance by fabricating Cr_2AlC MAX-phase coatings with a strong $(11\bar{2}0)$ prism plane texture, achieved via synchronized pulsed HiPIMS deposition. As a control, a texture-free, equiaxed Cr_2AlC coating was also prepared. Following a 5 h exposure to a simulated thermal–salt–steam environment at 600 °C, the textured coating demonstrated exceptional corrosion resistance, forming a corrosion scale that was only one-third the thickness of its equiaxed counterpart. Mechanistic investigations revealed that the Prism-plane coating orientation accelerates the formation of a dense, uniform amorphous Al_2O_3 scale, which acts as an effective barrier against corrosive species. These findings underscore the pivotal role of crystallographic orientation in environmental durability, offering a pathway to design high-performance MAX-phase coatings for extreme service conditions.

1. Introduction

Compressor blades used in carrier-borne aircraft and marine engines face severe thermal-salt-steam corrosion in marine environments, particularly from NaCl and water vapor. At elevated operational temperatures (350–700 °C), solid NaCl deposits readily accumulate on blade surfaces, dramatically accelerating corrosion processes in steam environments, thereby precipitating premature component failure [1–3]. Although conventional MCrAlY (M = Ni and/or Co) coatings are widely employed to mitigate oxidation at high temperatures, they degrade rapidly under aggressive thermal-salt-steam conditions. Similarly, traditional carbon- or nitrogen-based hard coatings exhibit effective erosion and wear resistance but are inherently susceptible to oxidation and salt-induced deterioration at elevated temperatures. Addressing these limitations requires the development of novel coatings with inherent resistance to corrosive thermal-salt-steam environments.

Recently, MAX phase materials ($M_{n+1}AX_n$, where M is an early transition metal, A is a group IIIA/IVA-group element, and X is carbon or nitrogen) have garnered increasing interest due to their nano-laminated microstructure, notable electrical conductivity, thermal stability, and intrinsic self-healing capabilities [4–6]. Among these, Cr_2AlC has emerged as a prominent MAX-phase candidate owing to its covalent Cr–C bonds and relatively weak metallic Cr-Al bonds, facilitating the preferential and rapid formation of a protective Al_2O_3 layer. Additionally, Cr_2AlC displays excellent thermal expansion compatibility with both Ni-based superalloys and alumina scales, further enhancing its oxidation resistance through the synergistic presence of Cr and Al elements [7–10]. For instance, Wang et al. [11] reported Cr_2AlC coatings fabricated via hybrid arc/sputtering deposition, which developed dense Al_2O_3 interfaces beneath outer $(Cr, Al)_2O_3$ layers. Upon oxidation at 1000 °C for 40 h, pronounced Al enrichment at the coating/substrate interface transformed into a dense α-Al_2O_3 scale at 1100 °C, markedly augmenting oxidation resistance. Similarly, Shamsipoor et al. [12] demonstrated that Cr_2AlC coatings formed Cr-enriched Al_2O_3 layers

---

[*] Corresponding author.
[**] Corresponding author at: State Key Laboratory of Advanced Marine Materials, Zhejiang Key Laboratory of Extreme-environmental Material Surfaces and Interfaces, Ningbo Institute of Materials Technology and Engineering, Chinese Academy of Sciences, Ningbo 315201, China.

E-mail addresses: wangzy@nimte.ac.cn (Z. Wang), kepl@nimte.ac.cn (P. Ke).

https://doi.org/10.1016/j.corsci.2025.113395
Received 9 July 2025; Received in revised form 27 September 2025; Accepted 6 October 2025

during hot-salt corrosion tests at 1223 K, confirming their protective efficacy. Therefore, Cr_2AlC MAX phase coatings have attracted considerable scientific and industrial attention as promising protective materials against corrosion in extreme environments [13–17]. Nevertheless, corrosion mechanisms of Cr_2AlC coatings under conditions involving steam and NaCl atmospheres—especially relevant to marine applications—remain insufficiently explored and warrant detailed investigation.

Due to their layered crystalline structure, MAX phases exhibit pronounced anisotropic behaviors, primarily arising from preferential migration of A-site atoms along basal planes rather than perpendicular to them [5]. For instance, A. Zuber et al. [18] demonstrated notable anisotropy in single-crystal Cr_2AlC samples oxidized at 1200 °C for 2 h; thinner oxide scales formed on plate surfaces oriented parallel to the basal plane compared to thicker oxides on plate edges oriented perpendicular to it. In addition, Ma et al. [19] reported that Cr_2AlC coatings with a preferred (103) orientation formed protective oxide passivation films more readily, thereby significantly enhancing corrosion resistance in simulated proton exchange membrane fuel cell (PEMFC) environments. Xu et al. [20] investigated oxidation behavior of textured Ti_3AlC_2 ceramics between 1000 and 1300 °C. The textured top surfaces, oriented parallel to the basal planes and perpendicular to the *c*-axis, developed dense, passivating Al_2O_3 layers owing to accelerated outward diffusion of Al along the (000*l*) planes. In contrast, surfaces without preferred orientation developed porous oxide layers composed predominantly of TiO_2 and Al_2TiO_5 at 1473 K. Therefore, these findings highlight that tailoring the growth of MAX phase coatings with a strong prism plane preferred orientation is critical for enhancing their corrosion and oxidation resistance

In this study, we synthesized highly textured Cr_2AlC MAX-phase coatings exhibiting a pronounced $(11\overline{2}0)$ preferred orientation—where the layered MAX-phase structure aligns perpendicular to the substrate—using high-power impulse magnetron sputtering (HiPIMS) coupled with synchronized pulsed substrate bias. Additionally, Cr_2AlC coatings with random orientation were deposited onto GH4169 superalloy substrates via a two-step approach combining HiPIMS deposition and subsequent vacuum annealing under identical conditions. Corrosion mechanisms of both coatings were systematically investigated at 600 °C under aggressive thermal–salt–steam coupled environments. Through comparative analysis, we elucidated the significant influence of the $(11\overline{2}0)$ preferred orientation on the high-temperature corrosion resistance of Cr_2AlC coatings.

2. Experimental procedure

2.1. Coating preparation

In this study, two types of Cr_2AlC MAX phase coatings were prepared: one with a preferred orientation and one without. For simplicity, the coating exhibiting a $(11\overline{2}0)$ preferred orientation is referred to as the Cr_2AlC $(11\overline{2}0)$ coating, while the one without a preferred orientation is designated as Cr_2AlC equiaxed coating. The substrate used was GH4169 superalloy (composition in wt%: 19.00 Cr, 52.50 Ni, 3.00 Mo, 0.50 Al, 0.95 Ti, 0.50 Co, 0.06 C, balance Fe). Substrates measuring 20 × 10 × 0.8 mm were mechanically ground using SiC paper (400–3000 grit), polished with 0.5 μm diamond paste to a mirror finish, and ultrasonically cleaned in acetone and ethanol for 10 min each.

2.1.1. Cr_2AlC $(11\overline{2}0)$ coating

A custom magnetron sputtering system equipped with multi-target sources was employed to deposit the Cr_2AlC MAX phase coating. Co-sputtering utilized two HiPIMS power supplies connected to a CrAl target (CrAl = 60:40 at%) and a graphite target, respectively. A synchronized pulsed bias of –100 V was applied, with two waveform generators precisely controlling the pulse sequence. The CrAl target was pulsed for 50 μs, followed by a 100 μs bias discharge, and then a 100 μs delay before pulsing the graphite target—details illustrated in Fig. 1 (Step 1). Deposition was conducted at 600 °C under a pressure of 0.6 Pa for 6 h, with the substrate rotating at 10 rpm to improve coating uniformity. Detailed deposition parameters are summarized in Table 1. Before deposition, a synchronized pulsed bias of –900 V was applied with the CrAl HiPIMS source active to promote ion bombardment. This step facilitated the formation of a CrAl transition layer via energetic Cr and Al ion implantation. The etching process was conducted at 200 °C for 20 min, with the graphite target deactivated throughout.

2.1.2. Cr_2AlC equiaxed coating

To evaluate the influence of crystallographic orientation on corrosion performance, an equiaxed Cr_2AlC MAX phase coating without preferred orientation was fabricated following a reported two-step procedure in our previous work [21]. During the first step, a HiPIMS power supply was applied to a composite CrAl target (CrAl = 60:40 at %), while the graphite target was driven by a DC power supply to balance the sputtering rates of Cr, Al, and C. Subsequent ex-situ annealing was performed in a quartz-tube furnace to crystallize the as-deposited amorphous film. Annealing was conducted at 600 °C for 2 h under a vacuum of 2×10^{-3} Pa with a heating rate of 10 °C/min. After annealing, samples were cooled to room temperature under natural convection.

2.2. Corrosion test

The thermal–salt–steam corrosion protocol was designed to simulate the aggressive service conditions encountered by compressor blades of carrier-based aircraft, where solid NaCl accumulates on blade surfaces and operational temperatures reach 600 °C in humid marine environments. The simulation was conducted in two steps:

Prior to salt deposition, the coated samples were thoroughly dried, weighed, and their surface areas precisely measured. The specimens were subsequently heated to 150 °C on a temperature-controlled stage. A 25 wt% NaCl aqueous solution, prepared with deionized water, was continuously and uniformly sprayed onto the heated surfaces. Rapid evaporation of water facilitated solid NaCl deposition. The mass gain from salt accumulation was recorded after each spraying cycle to control the areal salt loading. Deposition was repeated until a uniform NaCl layer of 1 ± 0.1 mg•cm^{-2} was achieved, as illustrated in Step 2 of Fig. 1.

The salt-laden samples were exposed to 600 °C in a tube furnace connected to a water vapor generator (Step 3, Fig. 1). Once thermal and flow stability were established, water vapor was introduced at 1 mg/min until uniform distribution was confirmed throughout the furnace. Samples were then inserted and maintained under these conditions for a fixed duration. After exposure, they were air-cooled to ambient temperature, completing the corrosion cycle.

2.3. Characterization methods

The phase structure of the as-prepared coating was characterized by X-ray diffraction using a D8-Advance diffractometer (Bruker, Germany) with Cu Kα radiation (wavelength $\lambda = 1.5406$ Å). Measurements were performed over a diffraction angle (2θ) range from 5° to 90°, at a scan rate of 0.5°/min. The surface morphology of the coating was examined by scanning electron microscopy (SEM, S-4800, Japan), transmission electron microscopy (TEM), including selected-area electron diffraction (SAED) and high-resolution TEM (HRTEM). The grain size within the Ti_2AlC coating was estimated using TEM dark-field (DF) and scanning TEM low-angle annular dark-field (STEM-ADF) imaging. Energy dispersive X-ray spectroscopy (EDS) maps and line scans across the passive film to the coating were obtained in scanning TEM high-angle annular dark-field (STEM-HADDF) mode with an EDS detector. TEM specimens were prepared using a focused ion beam (FIB, Helios-G4-CX, Thermo Scientific). A protective Pt layer was deposited on the TEM

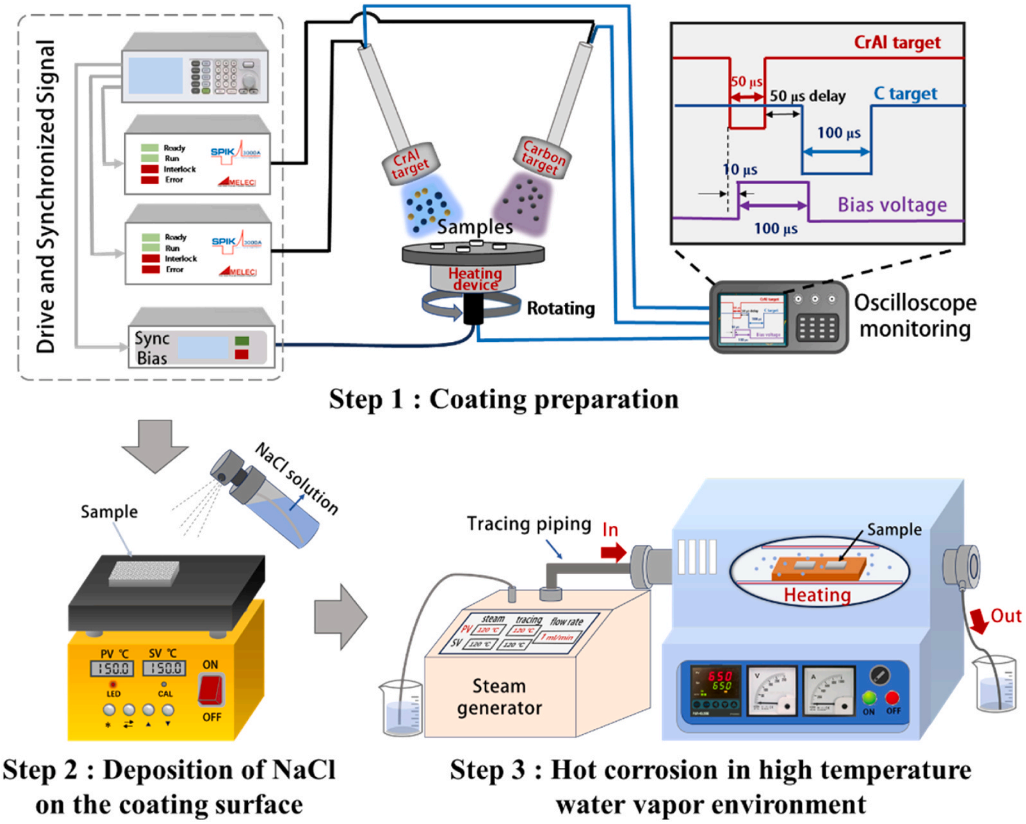

Fig. 1. (a) Schematic diagram of the deposition system of the Cr_2AlC $(11\bar{2}0)$ coating; (b) The process of NaCl deposition on the coating surface; (c) Schematic diagram of the thermal–salt–steam coupled corrosion process.

Table 1
Cr, Al ion etching and Cr_2AlC MAX phase coating deposition parameters.

Deposition parameters	CrAl target			C target			Bias			P(Pa)	T(°C)	Ar (sccm)
	Duty Ratio (%)	F(Hz)	P(W)	Duty Ratio (%)	F(Hz)	P(W)	Duty Ratio (%)	F(Hz)	U(V)			
Ion etching	2.5	500	105	-	-	-	-	-	−900	0.6	300	20
Cr_2AlC	2.5	500	105	5	500	100	5	500	−100	0.6	600	20

sample of the passive film before cutting to prevent scaling of the oxide layer.

The adhesion strength of the Cr_2AlC coatings deposited on GH4169 substrates was determined by scratch tester (CSM Revetest, Switzerland) under constant load mode, where a diamond Rockwell conical indenter with an approximated apex angle of 120° and a curvature radius of 200 μm was used. During the progressive scratch test, the indenter was loaded continuously from 1 N to 40 N with a scratch speed of 1.00 mm/min. The critical load where the coating was completely peeled off was determined to be the adhesion strength.

3. Results and discussion

3.1. *Characterization of as-prepared Cr_2AlC MAX phase coating*

Fig. 2a presents XRD patterns of the Cr_2AlC coatings deposited on GH4169 substrates. Comparing diffraction data to the standard reference reveals that the Cr_2AlC $(11\bar{2}0)$ coating exhibits a pronounced preferred orientation, with a dominant peak precisely matching the $(11\bar{2}0)$ reference peak. In contrast, the two-step deposited Cr_2AlC coating displays multiple diffraction peaks aligned closely with the standard reference but lacks any distinct crystallographic preference. The absence of impurity-related peaks, apart from substrate signals, confirms the high purity and compositional integrity of the synthesized Cr_2AlC MAX phase coatings.

Fig. 2b and c demonstrate that both coatings exhibit smooth, dense, and uniform surfaces, devoid of typical arc-deposition-related defects such as coarse particulates [21] or microcracks. Notably, a prominent white particle is observed on the surface of the equiaxed Cr_2AlC coating (Fig. 2c), which is likely attributable to airborne contamination during deposition or sporadic arc discharges occasionally present in the HiPIMS process. Beyond general surface quality, the two coatings reveal distinct morphological features: the equiaxed Cr_2AlC coating displays a characteristic spherical, cauliflower-like texture, whereas the Cr_2AlC $(11\bar{2}0)$ coating presents a sharp, spike-like topography with more angular and faceted surface grains. These differences underscore the influence of crystallographic orientation on surface evolution during growth. To clearly demonstrate the cross-sectional morphologies of the as-deposited coatings, we deposited the coatings onto Si substrates and observed the fractured cross-sections. Distinct differences were observed between the two coatings, consistent with their respective surface morphologies. The Cr_2AlC $(11\bar{2}0)$ coating, fabricated via a one-step process, displays a highly textured columnar grain structure (Figs. 2b-1), whereas the Cr_2AlC equiaxed coating, prepared via a two-step method, exhibits a

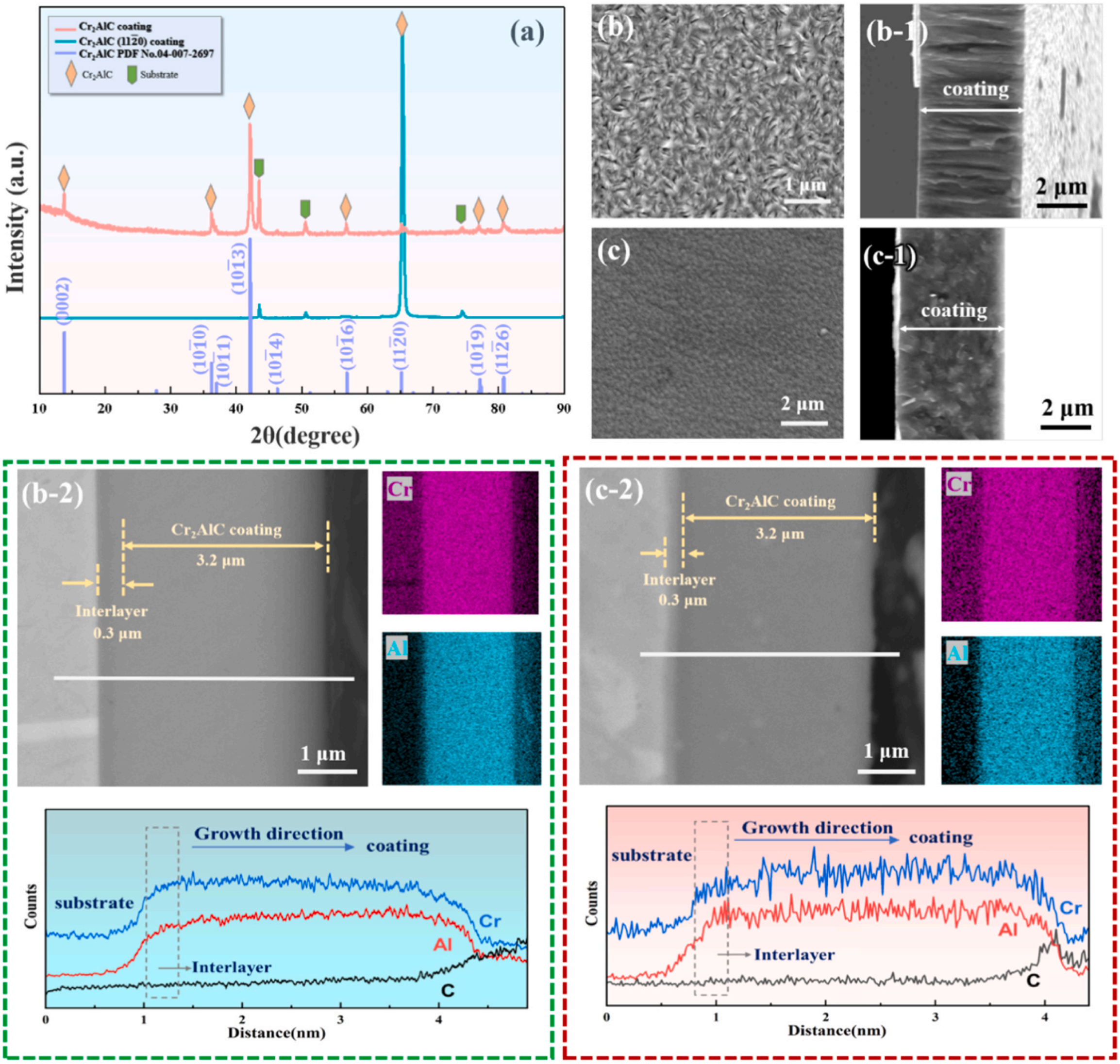

Fig. 2. (a) XRD pattern of the as-prepared Cr_2AlC coatings; Surface and fractured cross-sectional morphologies of Cr_2AlC (11$\bar{2}$0) coating (b, b-1) and Cr_2AlC equiaxed coating (c, c-1); Polished cross-sectional morphologies and elemental distributions of Cr_2AlC (11$\bar{2}$0) coating (b-2) and Cr_2AlC equiaxed coating (c-2).

randomly oriented equiaxed grain structure (Figs. 2c-1).

Cross-sectional SEM images and corresponding energy-dispersive spectroscopy (EDS) analyses (Figs. 2b-2, c-2) identify a well-defined three-layer architecture: an outer Cr_2AlC layer (~3.2 μm), an intermediate $CrAl_x$ interlayer (~0.3 μm), and the GH4169 substrate. Elemental distributions of Cr, Al, and C are homogeneous across the coating

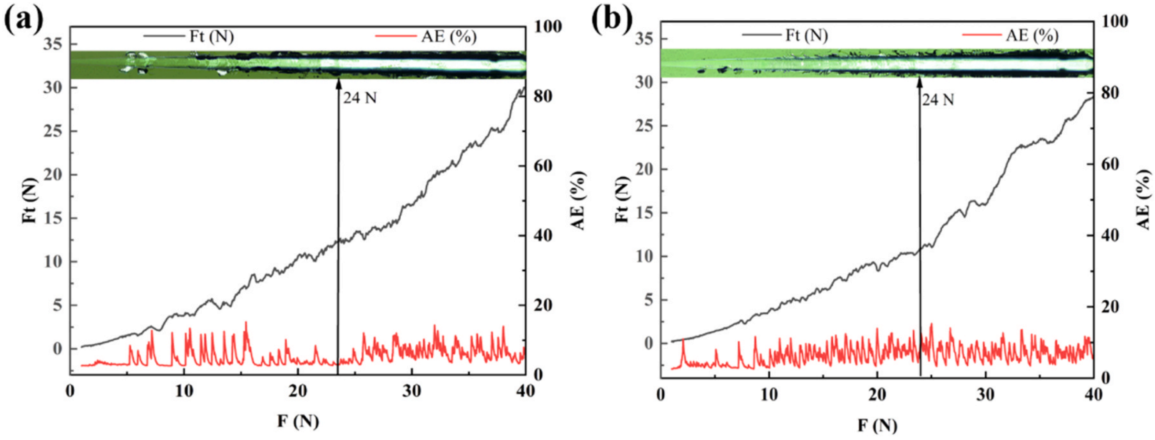

Fig. 3. The adhesion strength of the as-prepared: (a) Cr_2AlC equiaxed coating, (b) Cr_2AlC (11$\bar{2}$0) coating.

thickness, confirming uniform growth. The interface between coating and substrate appears sharp and defect-free, indicating robust interfacial bonding with no evidence of delamination or cracking. Such strong adhesion is attributed to enhanced atom diffusion and increased surface mobility induced by the high ionization rate and energetic ion bombardment characteristic of HiPIMS, consistent with prior studies [22].

Fig. 3 shows the adhesion strength of the as-prepared Cr_2AlC coating on the GH4169 substrates. During progressive load scratching, both coatings exhibited pronounced acoustic emission (AE) activity as the applied load approached 10 N, signifying the onset of extensive cracking and/or localized delamination at the coating surface. Upon further increasing the load to 24 N, in situ scratch track imaging (inset of Fig. 3) revealed significant coating spallation, exposing the underlying GH4169 substrate. These observations indicate that both coatings maintain strong interfacial adhesion, with a critical load for cohesive failure reaching approximately 25 N on GH4169 substrates.

3.2. *Phase composition after 5 h corrosion*

After 5 h corrosion testing, distinct differences in corrosion products were observed between Cr_2AlC equiaxed coating and Cr_2AlC $(11\bar{2}0)$ coating, as confirmed by XRD analysis (Fig. 4). The Cr_2AlC equiaxed coating exhibited a diverse array of corrosion products—including Cr_7C_3, $CrCl_2$, Al_2O_3, Cr_2O_3-indicative of pronounced chromium oxidation and Cl^- induced deterioration. In stark contrast, the Cr_2AlC $(11\bar{2}0)$ coating yielded solely Cr_2O_3. The absence of detectable Al_2O_3 phases in the XRD results indicates that the amount of Al_2O_3 formed is either below the detection limit of the technique or present in an amorphous state. In addition, the absence of chromium chlorides and carbides confirms negligible chloridation and decomposition of MAX phase, highlighting the superior corrosion resistance imparted by the preferred $(11\bar{2}0)$ orientation. Conversely, the presence of complex corrosion products such as Cr_7C_3, $CrCl_2$, and Cr_2O_3 in the equiaxed coating underscores extensive chromium oxidation and severe chloride-induced degradation. Specifically, $CrCl_2$ formation indicates pronounced chloride ingress under synergistic NaCl–H_2O attack, promoting structural deterioration via active chloridation mechanisms and ultimately leading to accelerated coating failure [23]. To elucidate the mechanisms underlying the observed divergence in corrosion resistance, we systematically characterized post-corrosion coatings through combined surface and cross-sectional analyses.

3.3. *Surface composition and morphologies after 5 h corrosion*

Fig. 5a, b compares the surface morphologies of the Cr_2AlC $(11\bar{2}0)$ and equiaxed coatings after 5 h exposure to corrosive conditions. Large particles on the surface are residual NaCl deposits originating from the salt-spray process. Notably, the Cr_2AlC $(11\bar{2}0)$ coating exhibits a markedly smoother and denser surface morphology relative to its equiaxed counterpart, indicative of significantly suppressed corrosion. Pronounced differences in oxide morphology and compactness are evident between the two coatings. High-magnification imaging of the Cr_2AlC $(11\bar{2}0)$ coating reveals well-adhered, uniformly distributed flaky oxides with characteristic lateral dimensions of ~1 μm. EDS mapping and compositional analysis (Fig. 5) confirm these flakes to be Al-rich, accompanied by substantial amounts of Na and O, with relatively lower Cr concentrations. This suggests selective oxidation of Al under NaCl-containing vapor at high temperature, producing a robust and continuous Al-rich oxide layer that effectively impedes further diffusion of corrosive species.

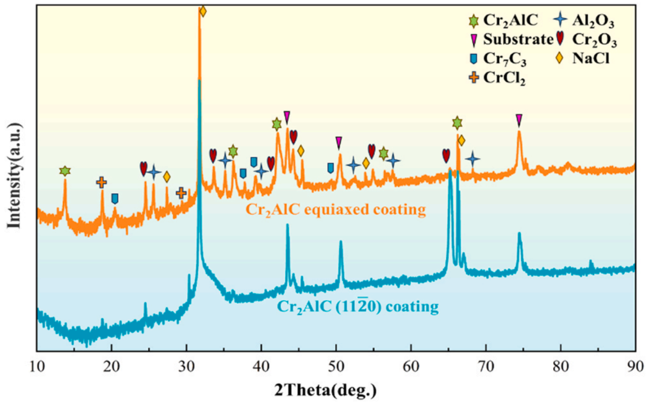

Fig. 4. XRD patterns of the Cr_2AlC $(11\bar{2}0)$ and Cr_2AlC equiaxed coatings after 5 h hot corrosion.

By contrast, the equiaxed Cr_2AlC coating displays widespread surface degradation, characterized by disordered, porous oxide layers with poor adhesion. EDS results indicate a complex oxide mixture predominantly composed of Cr and Al. Quantitative analysis of Area #1 (Fig. 5) shows a Cr:Al atomic ratio of 25.5:6.8—substantially deviating from the ~2:1 ratio observed in the textured coating—highlighting the dominance of Cr-based oxidation. Elevated oxygen content (~44 at%) and substantial levels of Na and Cl (~11 at% and 7 at%, respectively) further indicate deep infiltration and reaction with corrosive species. The resulting porous and inhomogeneous oxide layer lacks the structural integrity to prevent further degradation, accounting for the pronounced corrosion observed in the equiaxed sample relative to the highly textured Cr_2AlC $(11\bar{2}0)$ coating.

3.4. *Cross-sectional composition and morphologies after 5 h corrosion*

Fig. 6 presents the cross-sectional morphology of the equiaxed Cr_2AlC coating after corrosion. A protective Pt layer, deposited before focused ion beam (FIB) milling to prevent ion-beam damage, is not shown in Fig. 6. Elemental analysis (Fig. 6a; Table 2) reveals a ~1.2 μm thick corrosion scale, comprising an outer Al-rich oxide layer (~286 nm) and an inner, discontinuous CrC_x-rich sublayer (~930 nm) extensively infiltrated by secondary oxides. Within the interfacial corrosion region, voids in the CrC_x sublayer are partially filled with Al_2O_3, indicative of outward Al migration and oxide backfilling. Quantitative EDS data (Table 2) confirm the outermost oxide (Area #1) as stoichiometric Al_2O_3, with Al and O atomic concentrations of 32.1 at% and 60.4 at%, respectively. In contrast, Area #2 exhibits significant Al depletion (4.5 at%), consistent with substantial Al outward diffusion and the breakdown of the Cr_2AlC phase. This depletion leads to the formation of a Cr-rich carbide region, with a measured Cr:C atomic ratio of 63.1:22.5—closely matching the composition of Cr_7C_3—produced via the following oxidation reaction [17]:

$$Cr_2AlC(s)+O_2(g)\rightarrow Al_2O_3(s)+Cr_7C_3(s)+CO_x(g) \quad (1)$$

This reaction explains the Al depletion and the resulting structural changes in the corrosion layer. TEM analysis (Fig. 6b) further corroborates the presence of a crystalline Al_2O_3 surface layer and a Cr_7C_3-rich subsurface zone, in line with EDS findings. Further inward, the discontinuous Cr_7C_3 carbide regions are interspersed with amorphous oxides enriched in Na, Al, and Cr. As indicated by Fig. 6a, substantial accumulation of Na and Cl occurs preferentially at the interfaces between Cr_7C_3 and these internal amorphous oxide deposits, highlighting the limited barrier effectiveness of Cr-rich carbides against corrosive ion infiltration.

Even deeper into the coating (Area #5, Fig. 6a), notable concentrations of O (20.8 at%), alongside elevated Na and Cl contents, reveal substantial penetration and reaction of corrosive species, despite the presence of a surface Al_2O_3 barrier [24]. Thus, although a continuous Al_2O_3 scale eventually forms on the coating surface, significant ingress of corrosive elements (O, Na, Cl) occurs concurrently with outward Al

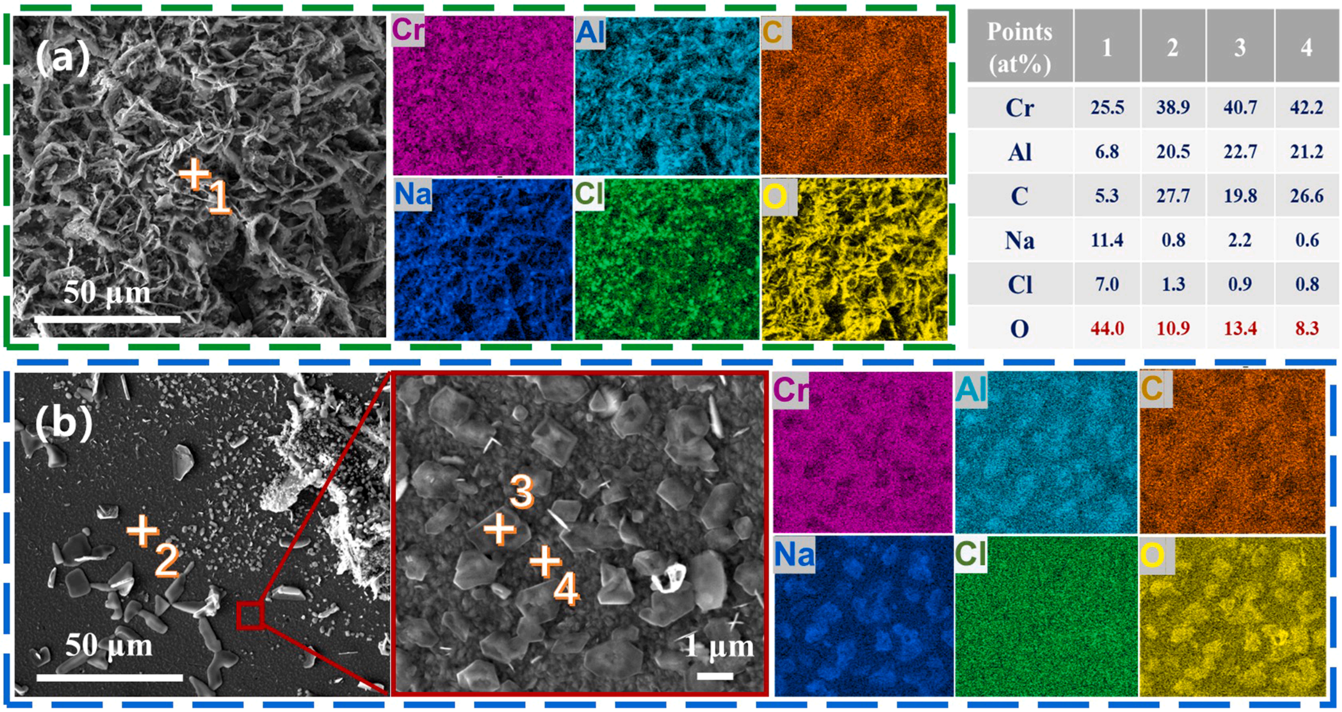

Points (at%)	1	2	3	4
Cr	25.5	38.9	40.7	42.2
Al	6.8	20.5	22.7	21.2
C	5.3	27.7	19.8	26.6
Na	11.4	0.8	2.2	0.6
Cl	7.0	1.3	0.9	0.8
O	44.0	10.9	13.4	8.3

Fig. 5. The surface morphologies and element distributions of the both coatings after 5 h corrosion: (a) Cr_2AlC equiaxed coating, (b) Cr_2AlC $(11\bar{2}0)$ coating.

diffusion. This early infiltration promotes extensive internal decomposition of Cr_2AlC to form a porous, Al-depleted Cr_7C_3-rich region, further exacerbating corrosion susceptibility.

Overall, this bidirectional transport—Al outward to form Al_2O_3, and aggressive species inward through evolving structural pathways—establishes a dynamic corrosion front. Although a dense Al_2O_3 scale gradually forms and impedes further attack, severe internal damage accumulates before the barrier becomes fully protective, ultimately compromising the coating's structural integrity.

Under identical hot corrosion conditions, Cr_2AlC $(11\bar{2}0)$ coating demonstrates markedly superior corrosion resistance compared to the equiaxed counterpart, as evidenced by cross-sectional analyses (Fig. 7). The resulting corrosion scale on the Cr_2AlC $(11\bar{2}0)$ coating is significantly thinner (~380 nm) and structurally more coherent. EDS mapping and compositional analysis (Fig. 7; Table 3) reveal a well-defined four-layer architecture: an outer Al-rich oxide layer (Area #1), an intermediate Na–Al–O mixed oxide layer (Area #2), a thicker subsurface Al_2O_3 layer (Area #3), and a narrow Al-depleted zone adjacent to the intact MAX phase (Area #4). Notable differences from the conventional equiaxed Cr_2AlC coating are as follows:

1) **Distribution of Corrosive Species (Na, Cl, O)**: The outer layers (Areas #1 and #2, Table 3) in the Cr_2AlC $(11\bar{2}0)$ coating contain higher levels of Na (~14 at%) and Cl (~2 at%) compared to equivalent regions in the equiaxed coating. However, the deeper uncorroded region (Area #5) shows substantially lower concentrations of Na, Cl, and O ions. Notably, the oxygen content is notably reduced to 5.5 at%, which highlights the effectiveness of the formed oxide layers in impeding corrosive species penetration.
2) **Characteristics of the Al-Depleted Region:** The equiaxed Cr_2AlC coating develops an extensive (~900 nm) Al-depleted zone enriched with Cr_7C_3, indicative of substantial Al outward diffusion. In contrast, the Cr_2AlC $(11\bar{2}0)$ coating features a notably thinner (~50 nm) and structurally uniform Al-depleted zone without evident Cr_7C_3 formation. This homogeneous Al diffusion ensures consistent and stable formation of protective Al_2O_3, contrasting starkly with the compromised corrosion resistance caused by the extensive Al-depleted zone in the equiaxed coating.
3) **Structural Characteristics of Al_2O_3 Layers:** The Cr_2AlC $(11\bar{2}0)$ coating develops dual alumina layers—a thin outer amorphous Al_2O_3 layer and a thicker inner amorphous layer closer to the uncorroded coating. TEM analyses confirm that these layers are predominantly amorphous, containing minimal Cr_7C_3 only at the interface, a result of limited local aluminum depletion [22]. The amorphous nature is attributed to the strongly preferred crystallographic orientation, which accelerates Al diffusion—particularly in this case, where weakly bonded, high-mobility Al atomic planes are aligned perpendicular to the substrate. This configuration promotes the ultrafast formation of a dense alumina layer, precluding sufficient atomic rearrangement for crystalline phase development.

The crystallinity of the Al_2O_3 scale exhibits a pronounced dependence on the underlying microstructure. In the Cr_2AlC $(11\bar{2}0)$ coating, the uniform grain orientation facilitates rapid and spatially homogeneous aluminum diffusion, which promotes the formation of amorphous Al_2O_3. This amorphous oxide is characterized by a low density of grain boundaries and structural defects, yielding a compact and continuous barrier that effectively inhibits the ingress of corrosive species [19]. In contrast, the random grain orientation in Cr_2AlC equiaxed coatings leads to heterogeneous Al diffusion pathways, slower oxide growth rates, and the subsequent formation of crystalline Al_2O_3. The resulting oxide scale, with increased grain boundaries and defects, exhibits lower density and diminished protective capacity, contributing to its inferior corrosion resistance [25–27].

3.5. *Extending the corrosion time to 20 h*

Under identical thermal–salt–steam coupled corrosion extended to 20 h, notable differences in corrosion behavior between the highly textured Cr_2AlC $(11\bar{2}0)$ coating and the Cr_2AlC equiaxed coating were observed (Fig. 8). Cross-sectional analyses (Fig. 8a, b) highlight significant degradation of the equiaxed Cr_2AlC coating, characterized by extensive accumulation of corrosion products. Upon light mechanical

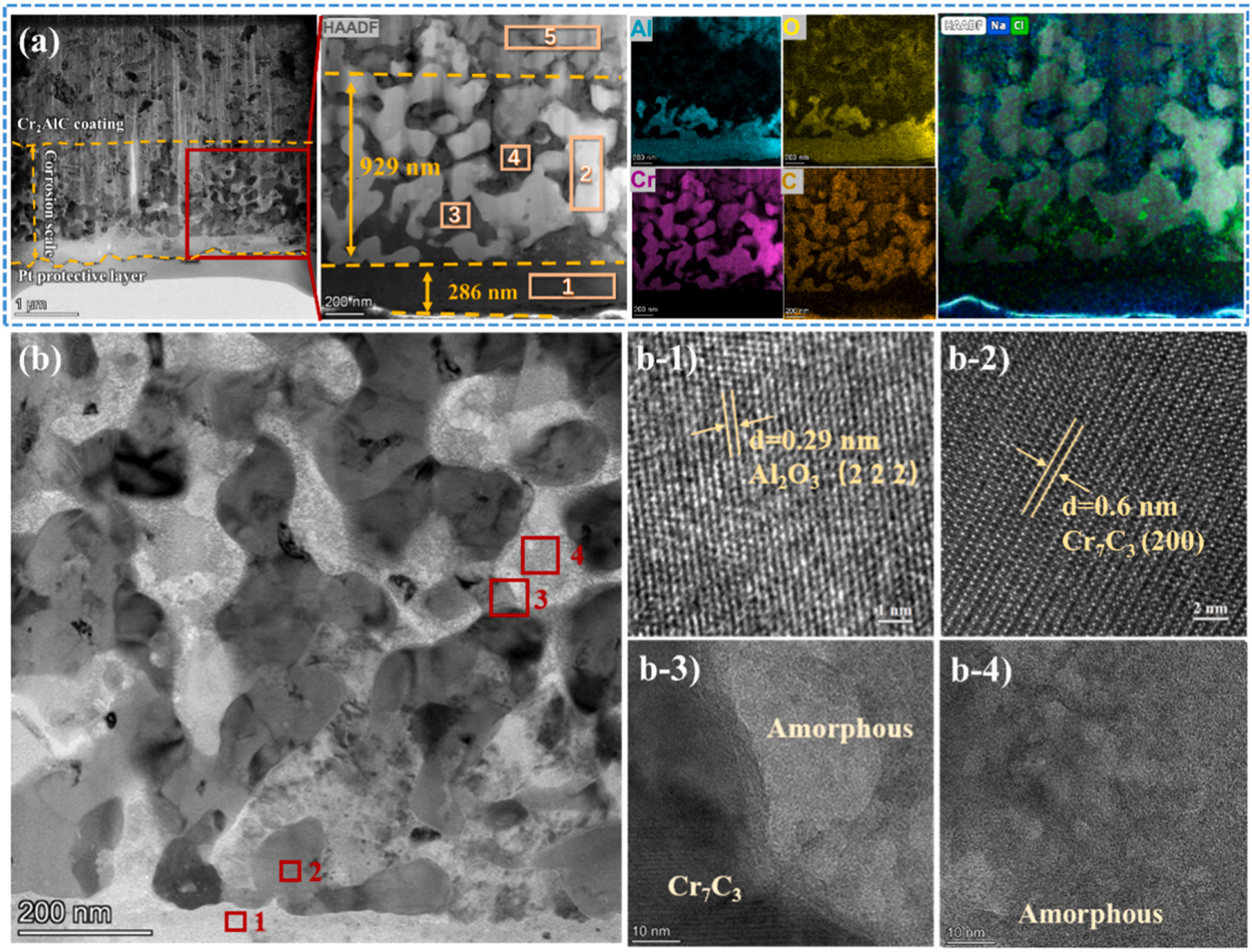

Fig. 6. Cr$_2$AlC equiaxed coating after 5 h corrosion: (a) Structure of FIB-prepared sample, representative high-magnification image, and corresponding EDS elemental mapping; (b) Cross-sectional bright-field plan-view TEM image; (b-1, b-2, b-3 and b-4) HRTEM images of regions 1, 2, 3 and 4 marked in (b).

Table 2
Elemental composition of the corresponding region in Fig. 6a.

Areas (at%)	Cr	Al	C	O	Na	Cl
#1	0.3	32.1	5.1	60.4	1.8	0.3
#2	63.1	4.5	22.5	8.8	0.8	0.3
#3	0.5	27.4	11.5	58.5	2.0	0.1
#4	6.8	6.5	24.0	56.5	5.7	0.5
#5	36.7	16.2	24.7	20.8	1.4	0.2

agitation, extensive spallation occurred, with over 50 % of the coating delaminating from the substrate. Elemental mapping (Fig. 8a) reveals pronounced inward oxygen penetration into the substrate and concurrent outward diffusion of substrate-derived Ni, indicating complete breakdown of the protective capability and structural integrity of the equiaxed coating.

In stark contrast, the Cr$_2$AlC (11$\bar{2}$0) coating remained structurally intact and chemically stable under the same conditions. SEM and composition analysis confirm that the coating exhibits a dense, adherent morphology with minimal surface degradation, limited to the formation of tiny nodules (Fig. 8c, d). Previous studies indicate that these nodules, typically composed of mixed oxides of Na, Cl, Al, and Cr, act as initiation sites for localized accelerated corrosion [22,28]. Elemental mapping clearly demonstrates minimal corrosion-induced elemental diffusion, retaining the original coating structure. These results demonstrate the superior performance of the Cr$_2$AlC (11$\bar{2}$0) coating, fabricated via synchronous pulse-biased HiPIMS deposition. The engineered crystallographic orientation promotes the rapid formation of continuous, protective alumina layers, enabling the coating to withstand harsh corrosive environments involving solid NaCl loading (1 mg•cm^{-2}) and 600 °C vapor exposure with exceptional durability.

3.6. Discussion on corrosion mechanism

To further elucidate the underlying corrosion mechanism, we examined the early-stage corrosion behavior by analyzing cross-sectional microstructures after 1 h exposure to hot corrosion conditions (Fig. 9). The Cr$_2$AlC (11$\bar{2}$0) coating rapidly developed a uniform, dense Al$_2$O$_3$ surface layer approximately 300–360 nm thick, effectively impeding corrosive species penetration. Although nanopores were observed within the Al$_2$O$_3$ layer, these features are attributed to ion-beam-induced artifacts introduced during FIB sample preparation and do not compromise the intrinsic protective performance of the coating. Cross-sectional comparisons after 5 h of corrosion (Fig. 7) revealed minimal growth (to ~380 nm), indicating remarkable stability of this protective oxide scale between 1–5 h of corrosion exposure. During this period, infiltrating O^{2-} preferentially reacted with Al, facilitating continuous and dense alumina scale formation.

Conversely, the equiaxed Cr$_2$AlC coating lacking a preferred orientation exhibited a thinner, non-uniform Al$_2$O$_3$ scale after 1 h (Figs. 9a, a-

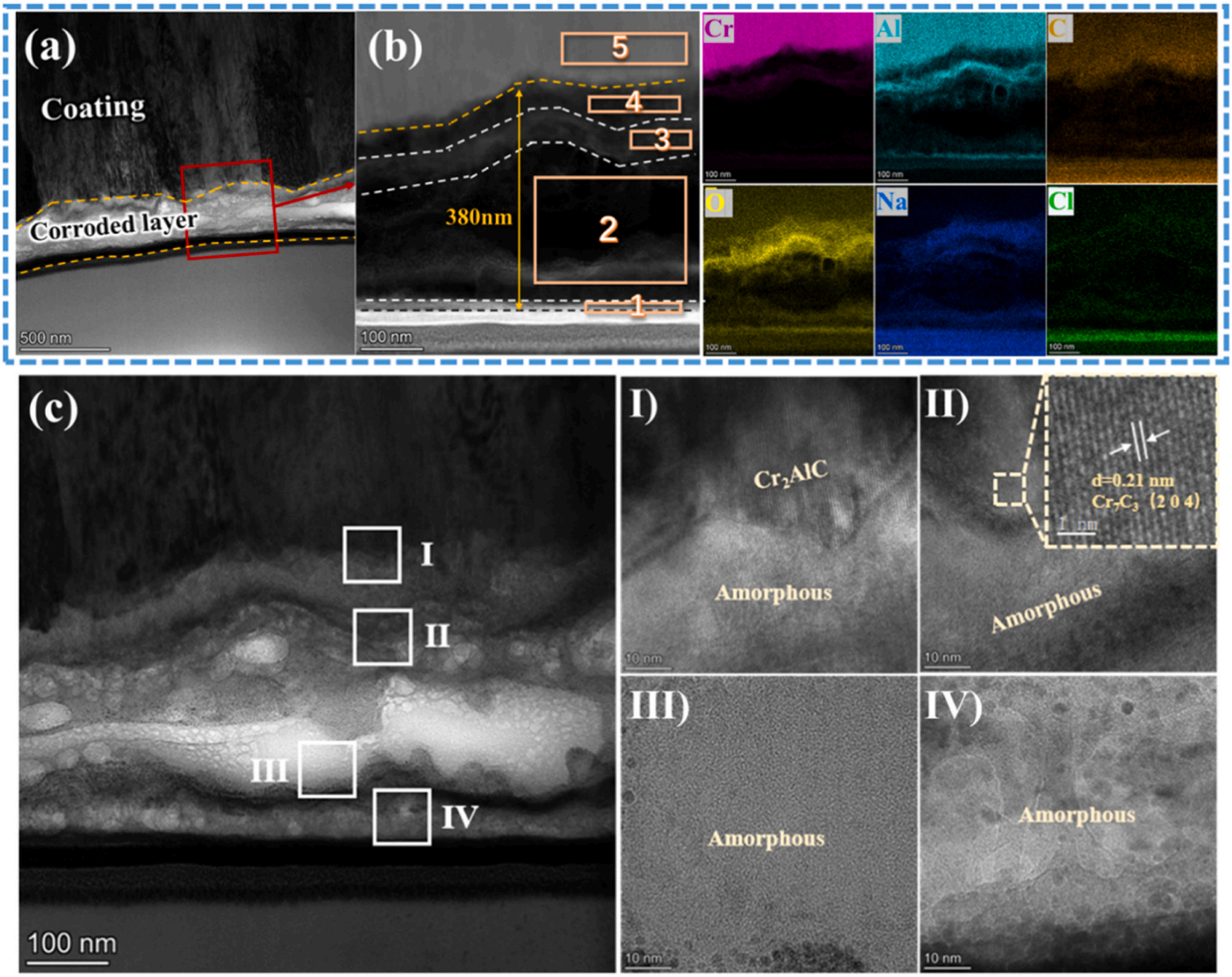

Fig. 7. Cr$_2$AlC (11$\bar{2}$0) coating after 5 h corrosion: (a) Bright-field cross-sectional TEM image of the coating after corrosion; (b) Magnified view of the selected region in (a) with corresponding EDS elemental mapping; (c) High-magnification image of the corrosion layer and HRTEM images of different regions.

Table 3
Elemental composition of the corresponding region in Fig. 7b.

Area (at%)	Cr	Al	C	O	Na	Cl
#5	63.8	19.7	8.9	5.5	1.9	0.2
#4	7.5	7.2	25.2	46.9	12.6	0.6
#3	7.7	27.3	10.5	49.8	4.0	0.7
#2	5.0	11.8	12.3	53.9	15.1	1.9
#1	6.5	27.3	7.8	48.4	9.3	0.7

1), accompanied by substantial and uniform infiltration of Cl ions into the coating structure. This early infiltration mechanism explains the pronounced enrichment of Na and Cl observed at the Cr$_7$C$_3$ interface after prolonged exposure (5 h, Fig. 6a). The inadequately protective, heterogeneous oxide layer failed to restrict the ingress of corrosive species ingress, accelerating Al depletion and structural degradation. As corrosion progressed to 5 h (Fig. 6), substantial Al depletion led to extensive Cr$_2$AlC decomposition, resulting in a porous, structurally compromised Cr$_7$C$_3$ layer ~920 nm thick. Consequently, the initial thin, irregular oxide film formed on the equiaxed coating proved insufficiently protective against prolonged aggressive corrosion.

Additionally, in the Cr$_2$AlC equiaxed coating lacking a preferred orientation, the random grain orientation induces heterogeneous Al diffusion behavior. Grains favorably aligned for Al transport exhibit accelerated outward diffusion, forming relatively thick Al-rich oxide layers (~300 nm) within 1 h. Conversely, poorly oriented grains hinder Al migration, resulting in ultrathin oxide layers (<80 nm) in adjacent regions. This spatial variation in oxidation behavior compromises the integrity of the protective scale. As expected, the Cr$_2$AlC (11$\bar{2}$0) coating—characterized by a high degree of crystallographic texture—enables uniform Al diffusion toward the surface, promoting the rapid formation of a dense and homogeneous Al$_2$O$_3$ layer. This directional diffusion not only facilitates oxide scale development but also maintains a dynamic equilibrium of Al concentration throughout the coating, thereby preventing the formation of localized Al-depleted zones. In the equiaxed coating, uncontrolled and localized Al depletion drives the decomposition of Cr$_2$AlC into Cr-rich phases, severely degrading the structural integrity and corrosion resistance of the coating. These findings underscore the crucial role of crystallographic orientation in modulating elemental diffusion, oxidation kinetics, and long-term stability under corrosive environments [29–31].

The corrosion mechanisms of both coatings are schematically illustrated in Fig. 10. At the initial stage, corrosion is primarily governed by the selective oxidation of Al. This process drives the formation of an Al$_2$O$_3$-rich surface scale and governs the subsequent structural evolution of the coatings. The Cr$_2$AlC (11$\bar{2}$0) coating exhibits markedly enhanced

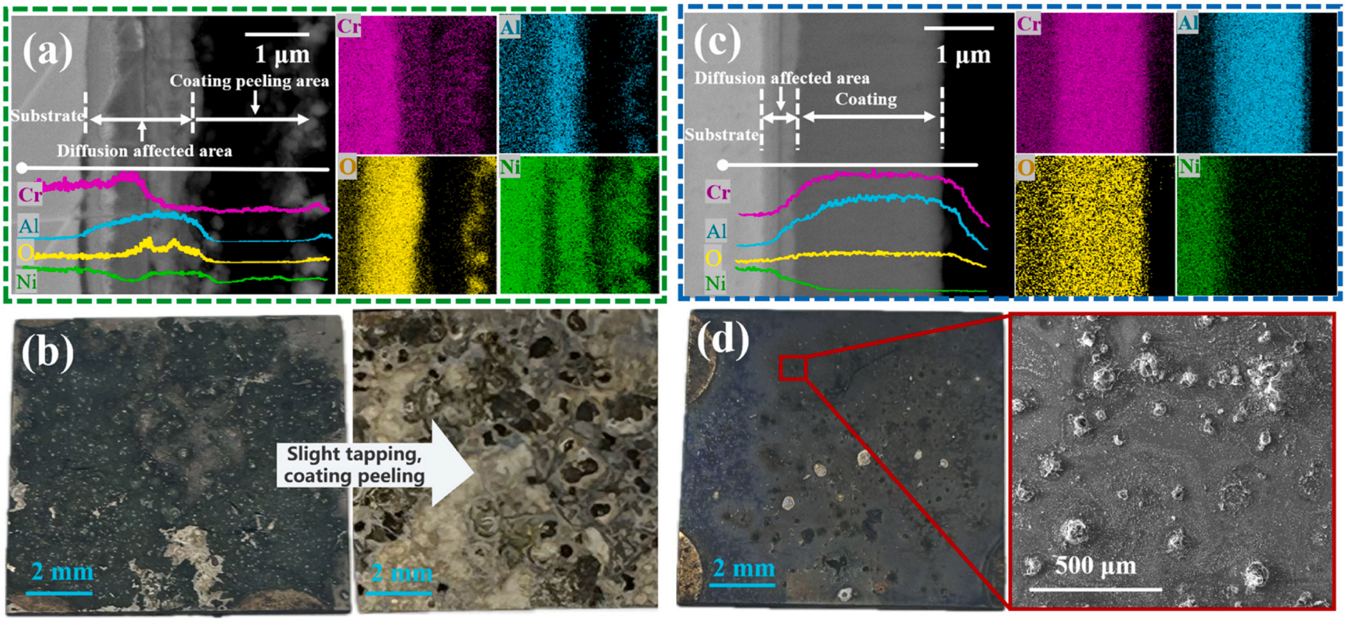

Fig. 8. Morphologies and compositions of the corrosion scale after 20 h corrosion for the Cr_2AlC equiaxed coating (a-b) and Cr_2AlC $(11\bar{2}0)$ coating (c-d). Cross-sectional morphologies and corresponding EDS results (a) and (c); Surface morphologies (b) and (d).

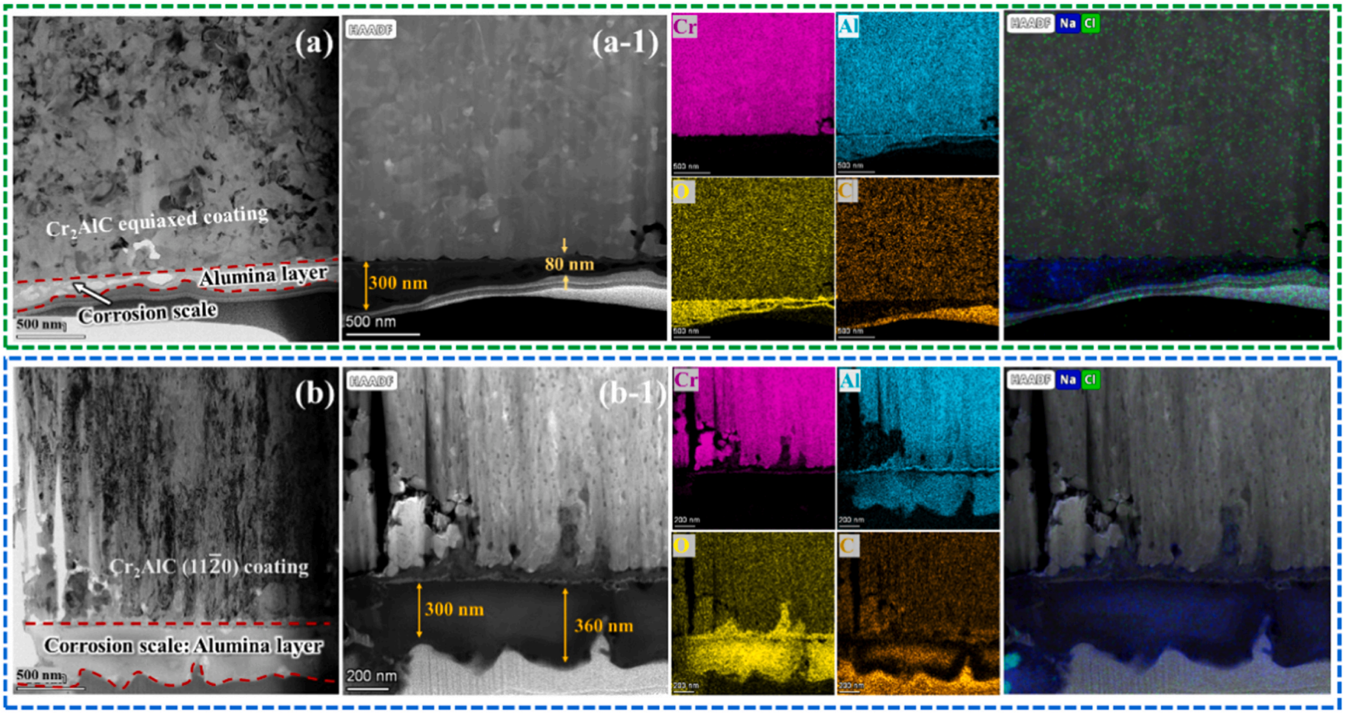

Fig. 9. Morphologies and compositions of the corrosion scale after 1 h corrosion: TEM bright-field image of the Cr_2AlC equiaxed coating (a) and Cr_2AlC $(11\bar{2}0)$ coating (b); STEM image and corresponding elemental mapping of the Cr_2AlC equiaxed coating (a-1) and Cr_2AlC $(11\bar{2}0)$ coating (b-1).

oxidation kinetics compared to its equiaxed counterpart, owing to the preferential Al diffusion along the (000*l*) crystallographic orientation. This directional transport facilitates the rapid formation of a continuous and uniformly thick Al_2O_3 scale. The structural alignment of grains across the coating ensures homogeneity in the oxide layer, minimizing local fluctuations in protective effectiveness. This dense oxide barrier significantly impedes the ingress of corrosive species such as Na^+, Cl^-, and O_2. Nevertheless, trace amounts of these species can permeate the outer Al_2O_3 layer and locally react to form a Na–Al–O mixed oxide phase, which marginally compromises the protective integrity of the surface scale. Consequently, limited oxygen transport persists, leading to the nucleation of a secondary Al_2O_3 layer deeper within the coating. This subsurface layer is accompanied by isolated and nanoscale Al-depleted zones, where Cr_2AlC decomposes into trace Cr_7C_3-undetectable in XRD due to its low content.

Conversely, the equiaxed Cr_2AlC coating forms a discontinuous and thickness-variable alumina layer during the early stages of corrosion (Fig. 9a). The randomness of grain orientations leads to spatially

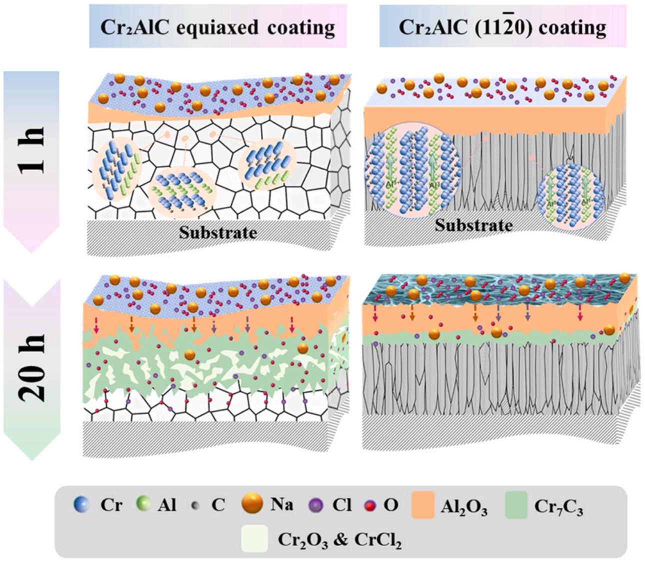

Fig. 10. Schematic diagram of the corrosion mechanism of the Cr_2AlC MAX phase coating under a thermal–salt–steam coupled environment at 600 °C.

inhomogeneous Al diffusion, creating an uneven oxide barrier that fails to effectively arrest corrosive penetration. Over prolonged exposure, the coating experiences extensive Al depletion, triggering decomposition of Cr_2AlC into a thick Cr_7C_3 rich zone beneath the oxide scale.

4. Conclusions

In summary, we have successfully fabricated high-purity Cr_2AlC MAX phase coatings with equiaxed grains and a high preferred (11$\bar{2}$0) orientation on the GH4169 substrate using the multi-target HiPIMS technique with synchronized pulse bias. Their corrosion behaviors were systematically studied under a thermal–salt–steam coupled environment at 600 °C with solid NaCl deposition of 1 mg•cm^{-2}. Results showed that after being exposed to thermal–salt–steam at 600 °C for 5 h, the textured (11$\bar{2}$0) coating significantly outperformed the equiaxed coating. The corrosion scale thickness measured at only one-third that of the equiaxed counterpart and the coating maintained structural integrity even after 20 h exposure. The superior performance of the textured (11$\bar{2}$0) coating is attributed to two key mechanisms: (1) rapid and homogeneous Al diffusion along the oriented structure, enabling the early formation of a compact, amorphous Al_2O_3 surface scale; and (2) effective suppression of Cr_2AlC decomposition and Cr_7C_3 formation by maintaining local Al concentration. In stark contrast, the equiaxed coating suffered from uneven Al diffusion, leading to porous oxide formation, deep Al depletion, and structural breakdown. This study highlights the importance of crystallographic orientation in governing corrosion resistance of MAX-phase coatings and provides a practical pathway to enhance coating performance under extreme environmental conditions.

CRediT authorship contribution statement

Kaiwei Yang: Methodology. **Kaihang Wang:** Investigation, Data curation. **Aiying Wang:** Writing – review & editing, Supervision, Funding acquisition. **Peiling Ke:** Writing – review & editing, Supervision, Funding acquisition. **Zhenyu Wang:** Supervision, Funding acquisition. **Xiaoyu Sun:** Writing – review & editing. **Shenghao Zhou:** Writing – original draft, Investigation, Data curation. **Kaixuan Xu:** Validation, Data curation.

Declaration of Competing Interest

The authors declare that they have no known competing financial interests or personal relationships that could have appeared to influence the work reported in this paper.

Acknowledgments

Kaixuan Xu and Shenghao Zhou contributed equally to this work. This work was financially supported by the National Natural Science Foundation of China (Nos. U22A20111 and 52171090), National Science Found for Distinguished Young Scholars of China (No. 52025014) and the Natural Science Foundation of Ningbo (2023QL049).

Data availability

Data will be made available on request.

References

[1] L. Fan, L. Liu, Z. Yu, M. Cao, Y. Li, F. Wang, Corrosion behavior of Ti60 alloy under a solid NaCl deposit in wet oxygen flow at 600 °C, Sci. Rep. 6 (2016) 29019.
[2] L. Liu, Y. Li, C. Zeng, F. Wang, Electrochemical impedance spectroscopy (EIS) studies of the corrosion of pure Fe and Cr at 600 °C under solid NaCl deposit in water vapor, Electrochim. Acta. 51 (2006) 4736–4743.
[3] Y. Tang, L. Liu, Y. Li, F. Wang, The electrochemical corrosion mechanisms of pure cr with NaCl deposit in water vapor at 600 °C, J. Electrochem. Soc. 158 (2011) C237.
[4] P. Eklund, M. Beckers, U. Jansson, H. Högberg, L. Hultman, The Mn+1AXn phases: materials science and thin-film processing, Thin Solid Films 518 (2010) 1851–1878.
[5] M. Guo, G. Cao, H. Pan, J. Guo, C. Chen, B. Zhang, J. Hu, Recent progress in synthesis of MAX phases and oxidation & corrosion mechanism: a review, Mater. Res. Lett. 12 (2024) 765–796.
[6] B. Rakhadilov, O. Maksakova, D. Buitkenov, M. Kylyshkanov, A. Pogrebnjak, V. Antypenko, Y.V. Konoplianchenko, Structural-phase and tribo-corrosion properties of composite Ti3SiC2/TiC MAX-phase coatings: an experimental approach to strengthening by thermal annealing, Appl. Phys. A 128 (2022) 145.
[7] Z. Lin, M. Li, J. Wang, Y. Zhou, High-temperature oxidation and hot corrosion of Cr2AlC, Acta Mater. 55 (2007) 6182–6191.
[8] H. Yang, Y. Pei, J.T.M. De Hosson, Oxide-scale growth on Cr2AlC ceramic and its consequence for self-healing, Scr. Mater. 69 (2013) 203–206.
[9] R. Pei, S. McDonald, L. Shen, S. van der Zwaag, W. Sloof, P.J. Withers, P. Mummery, Crack healing behaviour of Cr2AlC MAX phase studied by X-ray tomography, J. Eur. Ceram. Soc. 37 (2017) 441–450.
[10] L. Shang, P.K. Gokuldoss, S. Sandlöbes, M. Baben, J.M. Schneider, Effect of si additions on the Al2O3 grain refinement upon oxidation of Cr2AlC MAX phase, J. Eur. Ceram. Soc. 37 (2017) 1339–1347.
[11] Z. Wang, G. Ma, L. Liu, L. Wang, P. Ke, Q. Xue, A. Wang, High-performance Cr2AlC MAX phase coatings: oxidation mechanisms in the 900–1100°C temperature range, Corros. Sci. 167 (2020) 108492.
[12] A. Shamsipoor, M. Farvizi, M. Razavi, A. Keyvani, B. Mousavi, W. Pan, Hot corrosion behavior of thermal barrier coating on Cr2AlC and CoNiCrAlY substrates at 950 °C in presence of Na2SO4+V2O5 molten salts, Surf. Interfaces 21 (2020) 100679.
[13] M. Sokol, V. Natu, S. Kota, M.W. Barsoum, On the chemical diversity of the MAX phases, Trends Chem. 1 (2019) 210–223.
[14] J.-P. Palmquist, U. Jansson, T. Seppänen, P.Å. Persson, J. Birch, L. Hultman, P. Isberg, Magnetron sputtered epitaxial single-phase Ti3SiC2 thin films, Appl. Phys. Lett. 81 (2002) 835–837.
[15] D. Sauceda, P. Singh, A. Falkowski, Y. Chen, T. Doung, G. Vazquez, M. Radovic, R. Arroyave, High-throughput reaction engineering to assess the oxidation stability of MAX phases, npj Comput. Mater. 7 (2021) 6.
[16] G. Song, Y. Pei, W. Sloof, S. Li, J.T.M. De Hosson, S. Van der Zwaag, Oxidation-induced crack healing in Ti3AlC2 ceramics, Scr. Mater. 58 (2008) 13–16.
[17] W.Y. Ching, Y. Mo, S. Aryal, P. Rulis, Intrinsic mechanical properties of 20 MAX-phase compounds, J. Am. Ceram. Soc. 96 (2013) 2292–2297.
[18] A. Zuber, V. Gauthier-Brunet, J. Roger, J. Gonzalez-Julian, T. Ouisse, S. Dubois, Towards a better understanding of the high-temperature oxidation of MAX phase Cr2AlC, J. Eur. Ceram. Soc. 42 (2022) 2089–2096.
[19] G. Ma, D. Zhang, P. Guo, H. Li, Y. Xin, Z. Wang, A. Wang, Phase orientation improved the corrosion resistance and conductivity of Cr2AlC coatings for metal bipolar plates, J. Mater. Sci. Technol. 105 (2022) 36–44.
[20] L. Xu, D. Zhu, Y. Liu, T.S. Suzuki, B.-n Kim, Y. Sakka, S. Grasso, C. Hu, Effect of texture on oxidation resistance of Ti3AlC2, J. Eur. Ceram. Soc. 38 (2018) 3417–3423.
[21] Z. Li, Y. Zhang, K. Wang, Z. Wang, G. Ma, P. Ke, A. Wang, Highly dense passivation enhanced corrosion resistance of Ti2AlC MAX phase coating in 3.5 wt% NaCl solution, Corros. Sci. 228 (2024) 111820.

[22] Z. Wang, G. Ma, Z. Li, H. Ruan, J. Yuan, L. Wang, P. Ke, A. Wang, Corrosion mechanism of Ti2AlC MAX phase coatings under the synergistic effects of water vapor and solid NaCl at 600°C, Corros. Sci. 192 (2021) 109788.

[23] X. Li, S. Wang, G. Wu, D. Zhou, J. Pu, M. Yu, Q. Wang, Q. Sun, Oxidation and hot corrosion behaviors of MAX-phase Ti3SiC2, Ti2AlC, Cr2AlC, Ceram. Int. 48 (2022) 26618–26628.

[24] E.J. Opila, Volatility of common protective oxides in high-temperature water vapor: current understanding and unanswered questions, Mater. Sci. Forum. 461 (2004) 765–774.

[25] L. Qiang, X. Zhang, Y. Ai, Y. Zhuang, J. Sheng, H. Zhao, J. Ni, K. Yang, Crystallization behavior and thermal stability mechanism of plasma sprayed Al2O3-GAP amorphous ceramic coatings, J. Eur. Ceram. Soc. 42 (2022) 5108–5121.

[26] F. Xu, L. Luo, L. Xiong, Y. Liu, Microstructure and corrosion behavior of ALD Al2O3 film on AZ31 magnesium alloy with different surface roughness, J. Magnes. Alloy. 8 (2020) 480–492.

[27] A. Mavrič, M. Valant, C. Cui, Z.M. Wang, Advanced applications of amorphous alumina: from nano to bulk, J. NonCryst. Solids 521 (2019) 119493.

[28] F. Zakeri-Shahroudi, B. Ghasemi, H. Abdolahpour, M. Razavi, In situ coating and hot corrosion behavior of Cr2AlC MAX phase, J. Mater. Eng. Perform. 33 (2024) 5846–5858.

[29] M. Sokol, J. Yang, H. Keshavan, M.W. Barsoum, Bonding and oxidation protection of Ti2AlC and Cr2AlC for a Ni-based superalloy, J. Eur. Ceram. Soc. 39 (2019) 878–882.

[30] Y. Cheng, J. Chen, Y. Zhang, W. Liu, M. Nath, Y. Wei, W. Yan, S. Zhang, N. Li, Microstructure evolution of Cr2AlC MAX phase under a graphite bed between 1100 °C and 1500 °C, Ceram. Int. 49 (2023) 4987–4996.

[31] A. Zuber, V. Gauthier-Brunet, J. Roger, J. Gonzalez-Julian, T. Ouisse, S. Dubois, Cr2AlC high temperature oxidation under dry and wet air: understanding of the oxidation mechanism, J. Eur. Ceram. Soc. 43 (2023) 5159–5167.